

Hydrodynamics and Mass Transport in Wall Tube and Microjet Electrodes: Effect of Vortex Formation and Cell Geometry on Limiting Currents

James L. Melville,[†] Nafeesa Simjee,[‡] Patrick R. Unwin,[‡] Barry A. Coles,[†] and Richard G. Compton^{*,†}

Physical and Theoretical Chemistry Laboratory, Oxford University, South Parks Road, Oxford OX1 3QZ, U.K., and Department of Chemistry, University of Warwick, Coventry CV4 7AL, U.K.

Received: June 6, 2002; In Final Form: July 27, 2002

Using FIDAP, a finite element method simulation package, investigations into the effect of inlet wall thickness on the flow pattern occurring in the wall tube electrode or microjet electrode have been carried out. Simulation results show that vortex formation, observed above minimum solution velocity thresholds and missing from analytical treatments describing the flow, can have a critical effect on the hydrodynamics and hence on measured limiting currents. In addition, the current response for different-sized ring electrodes has been simulated at a range of speeds and suggests that the thickness of the jet tube wall and vortex formation can have an effect at both of these electrodes and radially offset microdisks. The latter are often used experimentally via the empirical maximization of observed currents. The dangers of applying approximate theory to these surprisingly complex devices are stressed.

Introduction

The microjet electrode (MJE)^{1–4} is part of a class of electrodes that can be termed “hydrodynamic ultramicroelectrodes”,⁵ where ultramicroelectrode properties combined with steady-state hydrodynamics give rise to unusually high mass-transport rates. In the MJE, a jet of electroactive fluid is impelled through a nozzle into a cell (normally filled with the same electroactive solution as in the jet). Under typical operating conditions, an ultramicroelectrode disk is placed directly beneath the jet of fluid, where a stagnation region occurs. The disk is much smaller than the size of the inlet, thus it represents a miniaturization of the wall tube electrode (WTE)⁶ rather than the wall jet electrode.⁷ An understanding of the hydrodynamic and mass transfer behavior at the MJE would be of great utility. In such complex cases, closed analytical solutions can be extremely difficult to obtain.

As an alternative, digital simulation via numerical solution of differential equations has proven to be a versatile and useful tool in the field of electrochemistry over the past few years. From a variety of available methods⁸ (e.g., orthogonal collocation,⁹ spline collocation,¹⁰ semi-integration,¹¹ and eigenvalue–eigenvector solutions¹²), the finite difference (FD)¹³ approach is the most popular because of its ease of application to a variety of electrode geometries and electrochemical techniques and the relative simplicity of the mathematics involved. However, it is difficult to use FD when attempting to simulate electrochemical processes taking place at geometries more complex than simple inlaid electrodes with regular geometries and algebraically well-defined hydrodynamics. For more challenging simulation problems, the finite element method (FEM)¹⁴ can be applied. However, the mathematics behind FEM is more complex; therefore, the use of FEM packages such as FIDAP,¹⁵ which requires the user to specify only the area of simulation, the

geometry, and any boundary conditions and then solves the equations that arise, can be very useful. In the past, FIDAP, which can be used to solve flow properties (via the Navier–Stokes equations) as well as diffusion problems, has been used successfully to simulate a variety of electrochemical techniques.^{16–19}

In previous papers in this series, the technique of using the FIDAP package to carry out a FEM simulation of MJE hydrodynamics and mass transfer was introduced.²⁰ Mass transport to a micrometer-scale electrode in the MJE configuration was subsequently investigated, and the relative effect of viscosity and the diffusion coefficient on the current was detailed.²¹ A further consideration is the effect of the geometry of the cell on the hydrodynamics and hence on the measured currents. Whereas a full investigation of this would require a 3D simulation, which would likely require unacceptable run times, some useful insights and conclusions can still be made from a 2D simulation when considering changes to geometry that maintain the 2D axial symmetry of the MJE model. Therefore, in this paper, we present results obtained by changing the thickness of the walls of the nozzle that acts as the means by which a jet of fluid is introduced into the MJE cell. Particular attention is paid to the effect of vortex formation, which is not accounted for in any previous treatment of the WTE or MJE.^{6,22}

Hitherto, only the simulated current response of a microdisk centered below the inlet has been studied. However, the disk can be displaced radially, outside of the stagnation region. Measuring the current as a function of radial displacement can provide useful information about the sensitivity of the current response to electrode placement and insight into the nature of mass transfer to a microdisk in an impinging jet setup.^{2,21} A simulation of an off-set electrode is a 3D problem, but a qualitative comparison could be made with that of a ring electrode, where increasing the size of the ring may be analogous to displacing the disk in some respects. Replacing the disk electrode with a microring in the MJE is similar to the operation of the radial flow microring electrode (RFMRE);^{23,24} however,

* Corresponding author. E-mail: richard.compton@chemistry.oxford.ac.uk.

[†] Oxford University.

[‡] University of Warwick.

in the following simulations, the thickness of the ring will be much thicker than that normally used in RFMRE experiments, and thus comparisons with the Levich equation for mass-transport-limited current-channel electrodes²⁵ are not justified.

Experimental Section

The MJE system was as described previously.²¹ In brief, it comprised a Pt disk UME (diameter 5 μm), and the ratio of electrode diameter to that of the surrounding insulator was 1:220 so that the electrode could be considered to sit in an infinite insulating plane. The electrode was mounted vertically, face up in the base of a purpose-built cell. This comprised a fully detachable Teflon base and a cylindrical glass body (diameter 10.4 cm, height 5 cm). The UME was positioned through a small hole (2 mm) in the base of the cell so that it protruded approximately 1.5 cm above the bottom of the cell but was submerged below the level of the solution. The cell could be drained, as required, by simply removing excess solution using a syringe.

Solution was delivered to the electrode via a tapered glass nozzle (i.d. 100 μm ; o.d. 120 μm). The nozzle was fabricated by drawing a borosilicate glass capillary (i.d. 1.16 mm, o.d. 2.0 mm; Harvard Apparatus, Kent, U.K.) to a fine point using a micropipet puller (Narishighe PB7, Tokyo, Japan) and then polishing to a flat finish on a home-built polishing wheel. Electrolyte solution was delivered at a series of volume flow rates using a precision dual-drive syringe pump (model no. U-74900-15, Cole-Palmer Instrument Company).

The nozzle was supported in a home-built capillary holder attached to a piezoelectric positioner (model no. P-843.30, Physik Instrumente, Waldbronn, Germany), which was used to control movement of the nozzle in the z -direction (normal to the UME) over a maximum expansion of 45 μm . The piezoelectric positioner was, in turn, mounted on a translational stage (M-015.00, Physik Instrumente), controlled by a differential micrometer (model DM-13). This facilitated a larger range of movement in the z -axis (25 mm) with micrometer resolution. Movement of the x and y stages, to which the nozzle was also connected, utilized DC-mike drives (M223.21 Physik Instrumente), controlled via a signal processor (C-852, Physik Instrumente) and 2-axis DC motor controller cards (C-842.20, Physik Instrumente). The positions of each axis were determined by digital encoders (MT25, Heidenhain, Germany) with a resolution of 0.1 μm .

All voltammetric measurements were made in a two-electrode arrangement, with a silver wire serving as a quasi-reference electrode (AgQRE) and the Pt disk UME, as the working electrode. Electrochemical measurements were made using a voltage scan generator (Colburn Electronics, Coventry, U.K.) and a home-built current follower (gains of 10^{-5} to 10^{-9} A/V). Data were recorded directly to a PC using a Lab-PC-1200 data acquisition card (National Instruments, Austin, Texas).

For the experiments reported herein, the end of the nozzle was typically about 500 μm from the electrode face. Line scans of transport-limited current as a function of relative nozzle position radially from the coaxial centerline position are presented. These were obtained from electrochemical images typically acquired over a region of approximately 400 μm square, with a series of unidirectional scans, usually with a step size of 5 μm between lines, with data acquired every 2 μm on a line. For all imaging experiments, the UME was held at a potential sufficient to oxidize the analyte of interest (IrCl_6^{3-}) at a transport-controlled rate.

All measurements were made in an air-conditioned laboratory (23 ± 0.5 °C). Solutions were prepared using Milli-Q reagent

TABLE 1: Geometry of MJE Models Simulated, with Dimensions Marked in Figure 1

Figure	4–6	7b
$r_{\text{elec}}/\Delta r$	5.65×10^{-3} cm	2.5×10^{-4} cm
H^a	(i) 10^{-1} cm (ii) 2×10^{-1} cm	5×10^{-2} cm
r_{T}	3.75×10^{-2} cm	5×10^{-3} cm
w	1.0575 cm	6×10^{-2} cm
l_{wall}^a	(i) 1.02 cm (ii) 1.625×10^{-1} cm (iii) 6.25×10^{-2} cm (iv) 1.25×10^{-2} cm	N/A
l_{exit}	2 cm	5×10^{-3} cm
$H_{\text{lower}}/H_{\text{upper}}$	(i) 10^{-1} cm (ii) 2×10^{-1} cm	N/A

^a Models were constructed with different inlet wall thicknesses and nozzle–electrode diameters.

water (Millipore Corp., resistivity 18 M Ω cm) and contained potassium hexachloroiridate(III) (1×10^{-3} mol dm $^{-3}$, Sigma-Aldrich), with potassium nitrate (0.1 mol dm $^{-3}$, purity 99.99%, Sigma-Aldrich) added as a supporting electrolyte.

Computational Approach

A detailed explanation of the finite element approach using FIDAP has been detailed in previous papers.^{20,21} The main strategy adopted was to divide the simulation into two parts: first, solve the flow problem at the MJE using an axially symmetric 2D radial cross section of the cell, and then simulate the diffusion to the electrode using a model of a much smaller area, with velocity values from the old model interpolated onto the new. This approach is justified at the low concentrations used as these will not affect the physical properties of the fluid, thus the flow is not coupled to the concentration distribution.

The degrees of freedom for each problem (either radial and axial velocity— u_r and u_z , respectively—or concentration, $c_{r,z}$) are solved at a series of nodes across the simulation area. These nodes make up the corners of a series of quadrilateral elements. The size and placement of the elements are controlled by defining quadrilateral areas (“mesh faces”) in the model and specifying the number and placement of nodes along the edges of the face. The elements are then generated by either a map or paving technique. The map mesh method requires an equal number of nodes to be placed on opposite sides of the mesh faces and produces a set of quadrilateral elements. The paving technique does not require an equal number of nodes on opposing faces and produces less-regular-shaped quadrilateral elements than a mapping technique. It was therefore used to smooth the transition between mapped mesh faces of different sizes.

The cell geometries modeled are given in Table 1, with a schematic of a model used to simulate the flow given in Figure 1 and with the position of the mesh faces indicated. The particular values of physical constants used to solve the equations are given in Table 2, corresponding to aqueous solutions. The interested reader is directed to the two previous papers in this series^{20,21} for a more detailed discussion of mesh face placement and meshing strategy. The model is axially symmetric around the line marked “centreline”, and calculations carried out by the simulation apply to the full 3D model that would result if the model were rotated around the centerline. The simplest model was the case where the thickness of the wall of the nozzle (by which the jet of fluid is introduced into the cell) was large enough that similar flow behavior near the electrode occurred no matter how much thicker the nozzle wall was made. This can be thought of as a “semi-infinite” nozzle-

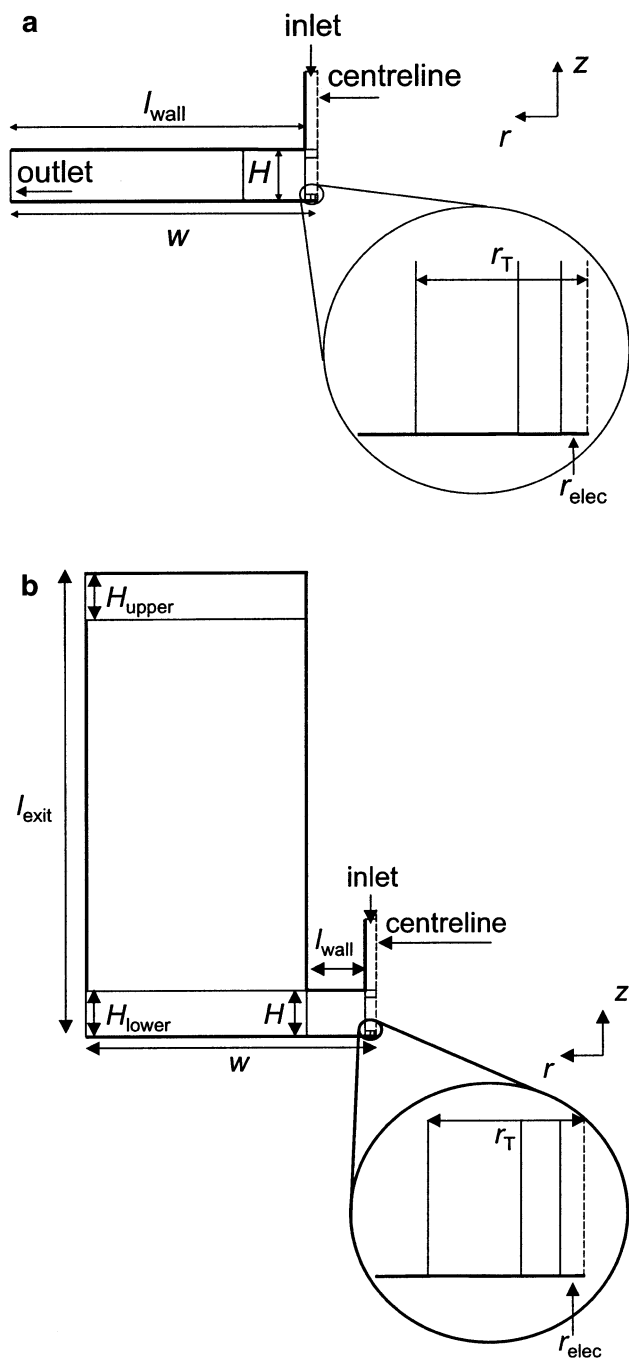


Figure 1. Outline of the axially symmetric model used to simulate flow with dimensions, position of mesh faces, and boundaries indicated for two geometries, (a) a wall of semi-infinite length and (b) a wall of defined thickness, allowing the positioning of outlets in either of two positions, upper or lower.

wall thickness. In this model, shown in Figure 1a, the nozzle wall extends outward all the way to outlet, creating an L-shaped cell section. The nozzle-wall thickness is marked as l_{wall} in Figure 1a. When a finite value of l_{wall} is defined, as shown in Figure 1b, extra mesh faces are introduced to simulate over the larger volume, taking in the full height of the cell. The extra height of the cell also allows for alternative placements of the outlet. In this work, the size of the outlet was kept constant, and its position altered between two extremes: a lower position, where the outlet is placed in the same position as in the semi-infinite wall case, and an upper position, where the outlet is the same distance from the electrode radially but is placed higher

TABLE 2: Physical Properties of the Solutions Simulated in the MJE

electroactive species	$\text{Fe}(\text{CN})_6^{3-}/\text{Fe}(\text{CN})_6^{4-}$	$\text{IrCl}_6^{3-}/\text{IrCl}_6^{2-}$
Figure	4–6	7b
temperature, T/K	298	296
viscosity, $\eta/\text{g cm}^{-1} \text{s}^{-1}$	0.00888	0.00888
density, $\rho/\text{g cm}^{-3}$	0.998	0.998
diffusion coefficient, $D/\text{cm}^2 \text{s}^{-1}$	6.5×10^{-6}	8.39×10^{-6}
bulk concentration, $c_{\text{bulk}}/\text{mol cm}^{-3}$	10^{-6}	10^{-6}

up in the cell. For given values of l_{wall} , the upper and lower cases can be calculated on identical meshes, the only change necessary being to the boundary conditions. The boundary conditions used to solve the flow problem in the MJE are summarized in Table 3.

The diffusion problem is solved by simulating over a reduced area, covered by two map mesh faces. Velocity values calculated using the larger mesh are interpolated onto the nodes making up this smaller submodel. The first mesh face extends radially to cover the radius of the electrode. The second mesh face accounts for any radial diffusion toward the edge of the electrode, for $r > r_{\text{elec}}$. By running simulations with the radial boundary of this mesh face at progressively larger intervals and noting the current, it was found unnecessary to simulate more than $200 \mu\text{m}$ away from the edge of the electrode in the radial direction. Any diffusion beyond this area affected the limiting current by $<0.1\%$. The axial extent of the submodel, z_{max} , was determined by first setting it equal to a value that would include all the diffusion to the electrode. This could be determined by inspecting the concentration values at various nodes away from the surface. The point at which the concentration reached bulk values, c_{bulk} , at $r = 0$ was set as z_{max} for all r . The interpolated velocity vectors were also examined. If, at the boundary, the vector indicates an axial component of the flow toward the electrode surface (i.e., $u_z < 0$), it was assumed that this flow was sufficient to replenish the bulk concentration, and a boundary condition of bulk concentration was applied to that boundary edge. Axial velocities are significant in the region directly below the jet; therefore, such conditions always occur for the simulation of a microdisk. However, in the case of a ring electrode (see below for details), the electrode surface will be placed further off-center as the ring size increases. As the electrode is placed further upstream, u_z becomes less negative. Where u_z is zero or becomes positive that boundary condition is no longer applied. Where this point occurs depends on the values of z_{max} and V_f for the particular simulation—generally, the region where $u_z < 0$ was confined to a smaller region below the jet as V_f was increased.

The only other boundary condition that it was necessary to specify was the concentration at the electrode surface, which was set to zero. These boundary conditions, which are all that are necessary to specify the diffusion problem in the simulation, are summarized in Table 4.

A ring electrode was also simulated using this technique. This was centered at the origin of the model; therefore, by moving the electrode in space along the wall in which it is embedded, when the axial symmetry is taken into account, ring electrodes of various sizes can be simulated. The parameters for defining the dimensions of the rings are shown in Figure 2. A similar model to the disk electrode was employed, except that radial diffusion can occur from both inside and outside the ring and therefore a third mesh face was added for the area where $r < r_a$. This was the same shape and size as the mesh face for $r > r_b$ (the equivalent of the mesh face for $r > r_{\text{elec}}$ in the microdisk case) and was scaled appropriately when r_a was less than $200 \mu\text{m}$. Where u_r was positive at the boundary of the third mesh

TABLE 3: Boundary Conditions for Calculation of Flow Problem in the MJE^a

parabolic flow at inlet	$0 \leq r \leq r_T$	$z = H + 500$	$u_z = (2\hat{U}/r_T^2) r^2; u_r = 0^b$
walls	$r = r_T$ $r_T \leq r \leq l_{\text{wall}}$ $r_{\text{elec}} \leq r \leq w$ $r = l_{\text{wall}}$ $l_{\text{wall}} \leq r \leq w$ $r = w$	$H \leq z \leq H + 3000$ $z = H$ $z = 0$ $H \leq z \leq 20\,000$ $z = 20\,000$ $0 \leq z \leq 20\,000$ $0 \leq z \leq 2000$	$u_z = 0; u_r = 0$
lower outlet	$r = w$		No boundary condition applies to an outlet; they are created by not specifying a “wall” boundary condition over the required distance.
upper outlet electrode centerline	$r = w$ $0 \leq r \leq r_{\text{elec}}$ $r = 0$	$18\,000 \leq z \leq 20\,000$ $z = 0$ $0 \leq z \leq H + 500$	$u_z = 0; u_r = 0$ $u_r = 0$

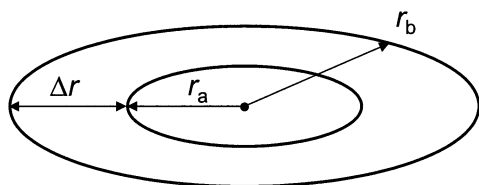
^a Coordinates are in units of μm . ^b \hat{U} is the average nozzle exit velocity.

TABLE 4: Boundary Conditions Used to Calculate the Limiting Currents in the MJE Simulation

microdisk			
bulk concentration at z_{max} if $u_z < 0$	$0 \leq r \leq r_{\text{max}}$	$z = z_{\text{max}}$	$c_{r,z} = c_{\text{bulk}}$
zero concentration at electrode surface	$0 \leq r \leq r_{\text{elec}}$	$z = 0$	$c_{r,z} = 0$
ring			
bulk concentration at z_{max} if $u_z < 0$	$0 \leq r \leq r_{\text{max}}$	$z = z_{\text{max}}$	$c_{r,z} = c_{\text{bulk}}$
bulk concentration at r_{min} if $u_r > 0$	$r_{\text{min}} \leq r \leq 0$	$z = z_{\text{max}}$	$c_{r,z} = c_{\text{bulk}}$
zero concentration at electrode surface	$r = r_{\text{min}}$	$0 \leq z \leq z_{\text{max}}$	$c_{r,z} = c_{\text{bulk}}$
	$0 \leq r \leq r_{\text{elec}}$	$z = 0$	$c_{r,z} = 0$

TABLE 5: Typical Values of z_{max} for a Ring of $\Delta r = 2.5\ \mu\text{m}$ and $0 \leq r_a \leq 0.02\ \text{cm}$ at Different Values of V_f

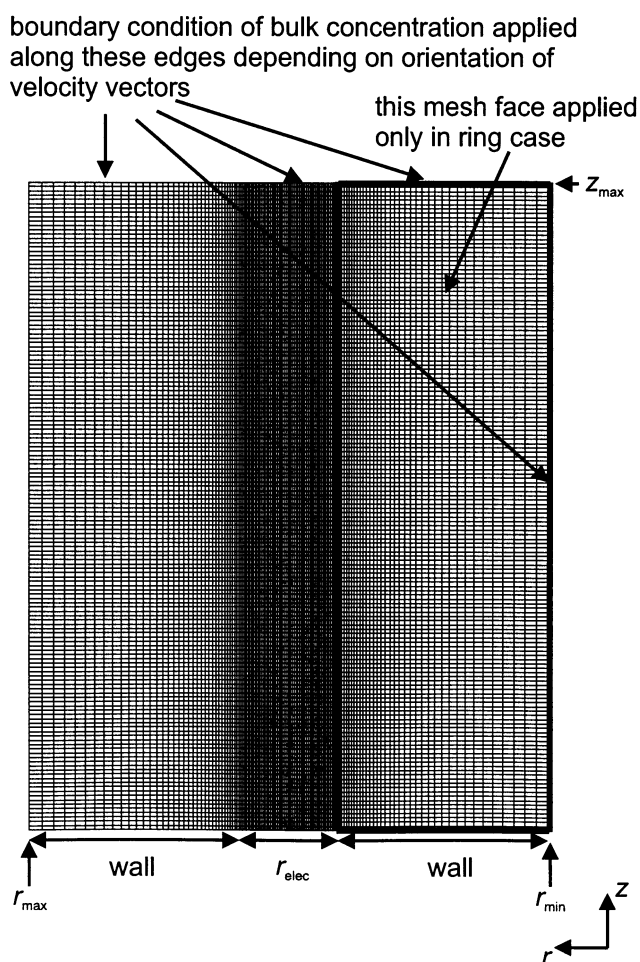
$V_f/\text{cm}^3\ \text{s}^{-1}$	8.33×10^{-3}	1.25×10^{-2}	2.50×10^{-2}	3.33×10^{-3}
$z_{\text{max}}/\mu\text{m}$	20	11	4	3

**Figure 2.** Ring electrode, with the dimensions necessary to define its geometry marked.

face marked as r_{min} in Figure 3, this indicated that the velocity of the solution could be expected to replenish the diffusion layer in this region, and hence a value of bulk concentration was applied at that boundary under those circumstances.

Illustrations of the meshes used to calculate the diffusion in disk and ring cases are given in Figure 3. Typical values of z_{max} used in the case of a ring with $\Delta r = 2.5\ \mu\text{m}$ for the range of flow rates simulated are given in Table 5. One value of z_{max} was acceptable at a given flow rate for all values of r_a simulated.

Numerical simulations were carried out with the finite element fluid dynamics package, FIDAP (version 8.52), executed on a 1.8-GHz Pentium 4 PC with 1 Gb of RAM. The flow models used 39 000 elements. The ring and disk diffusion submodels used 67 000 elements. Convergence values used by FIDAP in its solution software were set to 10^{-7} for the flow problem and 10^{-5} for the diffusion problem. Simulation required 20 min of CPU time for the flow solution and 5 min for the diffusion calculation.

**Figure 3.** Sample mesh used to calculate diffusion to a ring electrode. The disk electrode utilizes a similar model with the lower mesh face removed.

Results

Simulations were run to solve both flow and diffusion problems for a series of cells in order to probe the importance of the design of several different aspects of cell geometry. To begin with, solution properties were chosen to correspond to the behavior of a 1-mM aqueous solution of an $\text{Fe}(\text{CN})_6^{3-}/\text{Fe}(\text{CN})_6^{4-}$ couple at 298 K. The relevant values are listed in the first column of Table 2.

TABLE 6: Limiting Currents (10^{-8} A) at $V_f = 10^{-3}$ cm³ s⁻¹ for Differing Geometries

exit placement	$l_{\text{wall}} = 0.1625$ cm		$l_{\text{wall}} = 0.0625$ cm		$l_{\text{wall}} = 0.0125$ cm		$l_{\text{wall}} = 1.02$ cm (semi-infinite)
	upper	lower	upper	lower	upper	lower	
$H = 0.2$ cm	1.58876	1.58870	1.58835	1.58836	1.59172	1.59173	1.58870
$H = 0.1$ cm	1.94741	1.94819	1.94752	1.94830	1.94464	1.94503	1.94719

“Normal” Flow. Above a certain flow rate, the lateral movement of the fluid as it impinges on the electrode and flows away radially causes vortices to form in the cell. As it was anticipated that these might have an effect on the flow to the electrode, and hence the limiting current, simulations were initially run at a flow rate that was sufficiently slow to prevent vortex formation. For all the geometries given in Table 1, a V_f of 10^{-3} cm³ s⁻¹ met this criterion. Models of a MJE were constructed with two different values of H , the inlet–electrode separation: 0.1 and 0.2 cm. For each value of H , four MJE models were constructed, given by the geometries listed in Table 2, with different values of l_{wall} with the internal radius of the inlet r_T having a constant value of 0.0375 cm. The four values of l_{wall} used were 0.1625, 0.0625, 0.0125, and 1.02 cm, the latter value designated as being of semi-infinite thickness because it extended across the entire width of the cell, terminating only when the outlet was reached. There were two other possible choices when using a model involving the three finite values of l_{wall} and upper or lower placement of the exit, as marked in Figure 1b. Semi-infinite nozzle-wall geometry constrains the placement of the outlet into a lower position only.

Table 6 shows the simulated limited currents obtained at a flow rate of 10^{-3} cm³ s⁻¹ for the geometries mentioned above. The results show a difference of $<0.5\%$ between the highest and lowest currents obtained at a given inlet–electrode separation, no matter what exit placement or values of l_{wall} are chosen. When $l_{\text{wall}} = 0.1625$ cm, the discrepancy between the limiting currents obtained for either upper or lower exit placement are $<0.05\%$ of the values of the semi-infinite case. These results suggest that for normal flow conditions (i.e., no vortices) and for a microdisk placed directly under the inlet the limiting current is relatively unaffected by the thickness of the inlet wall and the exit placement, under the important proviso that the exit has been sized and placed so that it acts indistinguishably from an outlet of the same height that extends around the entire circumference of the cell.

Flow with Vortex Formation. Having shown that under normal flow conditions the limiting current is little affected by the exit placement and value of l_{wall} , a series of simulations were run at higher flow rates, where a vortex forms in the cell. Limiting currents were obtained for a series of flow rates from 10^{-3} to 10^{-1} cm³ s⁻¹ for the values of l_{wall} given above, and for two separate inlet–electrode separations, $H = 0.1$ and 0.2 cm. For all values of l_{wall} and all exit placements, the difference in limiting current when compared to the semi-infinite wall geometry was less than 2.1% and was largest at the thinnest nozzle wall ($l_{\text{wall}} = 0.0125$ cm). Limiting currents differed by less than 0.05% from the semi-infinite case when $l_{\text{wall}} = 0.1625$ cm. At any value of l_{wall} , the limiting current difference between the lower and upper exit placement was less than 0.06%.

To evaluate the effect of finite values of l_{wall} compared to the semi-infinite case, the discrepancy between the simulated limiting currents was calculated as

$$\Delta I_{\text{wall}} = (I_{\text{semi}}/I_w) - 1 \quad (1)$$

where I_{semi} is the simulated limiting current for the semi-infinite case and I_w is the current obtained with a finite l_{wall} value.

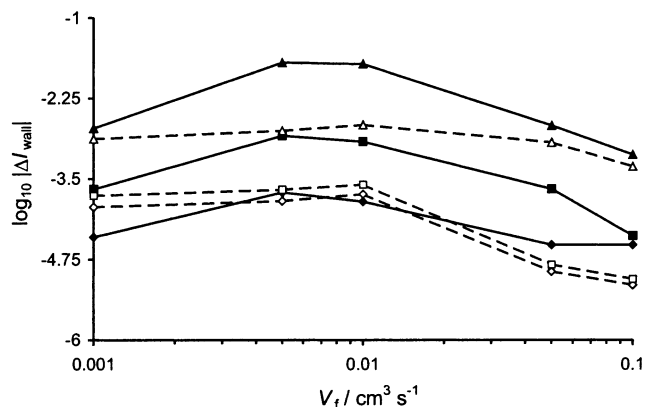


Figure 4. Effect of flow rate on the discrepancy between simulated limiting currents obtained for a number of cells with geometries of a finite inlet wall thickness and the currents obtained when the wall is 1.02-cm long, which is considered long enough to be of semi-infinite length, at a microelectrode of $\Delta r = 56.5$ μm . Data were obtained for the following geometries: $l_{\text{wall}} = 0.1625$ cm (\diamond), $l_{\text{wall}} = 0.0625$ cm (\square), and $l_{\text{wall}} = 0.0125$ cm (\triangle). Solid symbols represent currents for $H = 0.2$ cm, and open symbols, for $H = 0.1$ cm.

Plots of ΔI_{wall} against V_f for three different values of l_{wall} and two values of H are given in Figure 4. As can be seen, when $l_{\text{wall}} = 0.1625$ cm, for both $H = 0.2$ and 0.1 cm, limiting currents show a discrepancy of less than 0.1% for all flow rates simulated when compared with that of the semi-infinite wall case. As the nozzle-wall thickness is reduced, the discrepancy increases. For the thinnest wall ($l_{\text{wall}} = 0.0125$ cm) and $H = 0.2$ cm, the discrepancy is larger than 1% at some flow rates.

For all geometries, the same trend in ΔI_{wall} can be observed: the discrepancy is low at high and low flow rates (10^{-3} and 10^{-1} cm³ s⁻¹) but rises to a maximum in the region of 10^{-2} cm³ s⁻¹. To explain this pattern, a comparison of streamline contours in the region of the cell near the microdisk is necessary.

Figure 5 shows contours of constant streamlines at three flow rates: 10^{-3} , 10^{-2} , and 10^{-1} cm³ s⁻¹. The solid lines represent the contours in the case of the semi-infinite value for l_{wall} . The broken line represents the same contours when the wall is reduced to a thickness of 0.0125 cm and the exit is placed in the upper position. At the lowest speed, the effect of a thin wall is to cause the streamlines to shift their positions relative to those of the semi-infinite wall case. This deviation is smallest directly below the nozzle and decreases toward the electrode. At 10^{-2} cm³ s⁻¹ (Figure 5b), a vortex has been formed, and the effect of reducing the wall thickness is to shift the position of the vortex, causing a slightly larger effect on the positions of the streamlines than at the lower speed. At higher speeds (Figure 5c), a vortex is still present but has now moved further upstream, and the effect on the streamlines of reducing l_{wall} is much reduced in the area of the electrode. Inspection of the streamlines helps to explain the shape of the discrepancy in limiting currents given in Figure 4; at the highest and lowest speeds, the effect of the thinner wall is not noticeable in the region near the electrode, whereas at the intermediate speed, the vortex is closest to the electrode, and the change in contour shape due to a change in wall thickness is most pronounced in that region for this speed. It can be seen that the value of ΔI_{wall} reaches a maximum

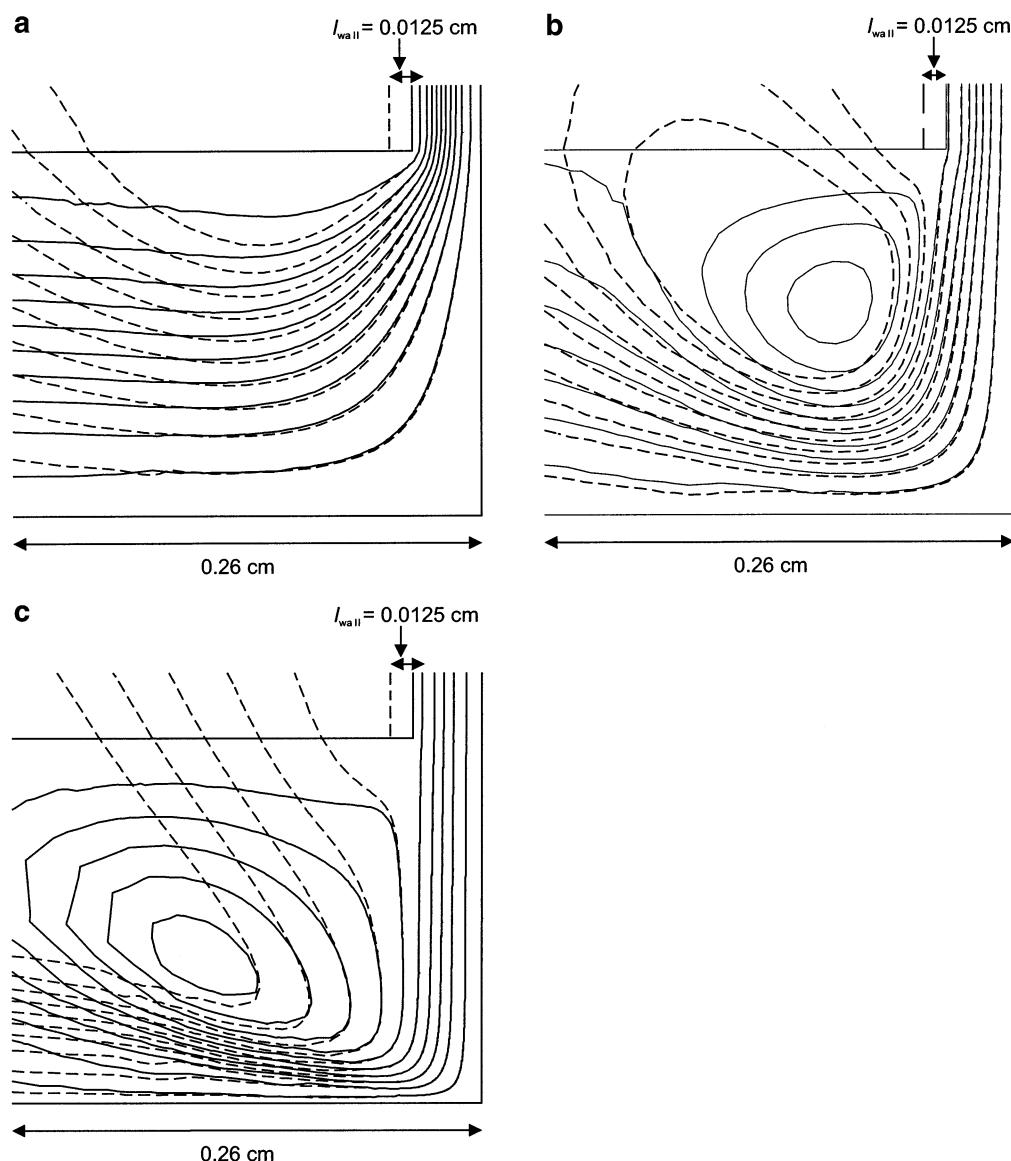


Figure 5. Streamline contours showing the shape of the flow profile for a region of the MJE near the electrode for V_f = (a) $10^{-3} \text{ cm}^3 \text{ s}^{-1}$, (b) $10^{-2} \text{ cm}^3 \text{ s}^{-1}$, and (c) $10^{-1} \text{ cm}^3 \text{ s}^{-1}$. Solid lines show the contours when $l_{\text{wall}} = 1.02 \text{ cm}$, and broken lines show the contours when $l_{\text{wall}} = 0.0125 \text{ cm}$.

slightly earlier at the larger nozzle–electrode separation, where $H = 0.2 \text{ cm}$. This correlates with the fact that vortex formation occurs at a lower value of V_f for the larger value of H . Hence, the maximum disruption of the flow profile occurs at a lower flow rate. The above discussion illustrates that vortex formation can have a noticeable effect on the current to a microdisk in the MJE, and the possibility of its formation must be carefully considered when designing the geometry of a cell. However, whereas the discrepancy in current is almost 2% in the case of the geometries that produce the two sets of contours shown in Figure 5b, Figure 4 shows that in general the effect of reducing l_{wall} results in much smaller changes in limiting currents.

Effect of Vortices on Radially Off-Set Electrodes. From Figure 5, it appears that changes to l_{wall} can change the flow profile at positions downstream from the area directly below the inlet. Therefore, offsetting the microelectrode radially might be able to probe these changes. Although a disk microelectrode that moved downstream would result in an asymmetrical model that would require a 3D approach, by simulating a ring electrode, the axial symmetry can be maintained—moving the electrode downstream would be equivalent to expanding the size of the

ring. Results for different-sized rings can be compared by normalizing with respect to an empirical equation given by Szabo²⁶ for calculating the steady-state diffusion current in stagnant solution for any size of ring:

$$I_{\text{ring}} = nFDc_{\text{bulk}}\pi^2 \frac{(r_a + r_b)}{\ln\left[\left(\frac{32r_a}{r_b - r_a}\right) + \exp\left(\frac{\pi^2}{4}\right)\right]} \quad (2)$$

where n is the number of electrons in the charge-transfer reaction, F is the Faraday constant, D is the diffusion coefficient of the electroactive species, and c_{bulk} is its concentration at bulk values. r_a and r_b are the inner and outer radii of the ring, respectively, as defined in Figure 2.

Equation 2 has been shown to be accurate in other investigations made previously by this group.²⁷ When $r_a = 0$, this equation becomes the familiar microdisk equation:

$$I_{\text{UME}} = 4nFDc_{\text{bulk}}r_{\text{elec}} \quad (3)$$

Use of this equation for the relevant geometry and conditions

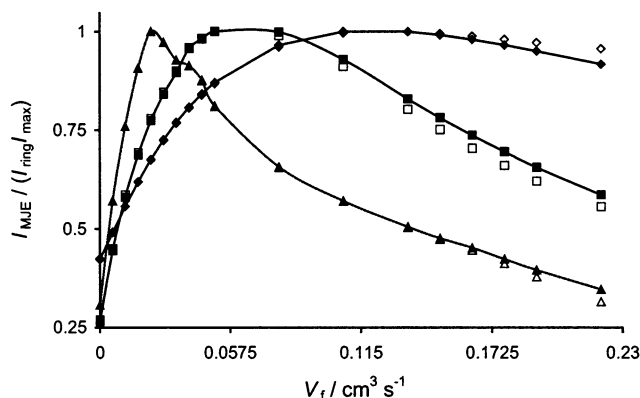


Figure 6. Simulated limiting currents, normalized with respect to the Szabo ring equation and maximum current obtained, for a series of increasing ring sizes with $\Delta r = 56.5 \mu\text{m}$ for $V_f = 10^{-3} \text{ cm}^3 \text{ s}^{-1}$ (\diamond), $V_f = 10^{-2} \text{ cm}^3 \text{ s}^{-1}$ (\square), and $V_f = 10^{-1} \text{ cm}^3 \text{ s}^{-1}$ (\triangle). Solid symbols represent currents obtained in the case of $l_{\text{wall}} = 0.0125 \text{ cm}$, and open symbols correspond to currents obtained for the semi-infinite l_{wall} .

given below gave errors of less than 0.2% when compared with the equation given by Symanski and Bruckenstein²⁸ in the limit of a very thin ring ($r_a/r_b > 0.91$):

$$I_{\text{ring}} = nFDc_{\text{bulk}}\pi^2 \frac{(r_a + r_b)}{\ln\left[16\left(\frac{r_b + r_a}{r_b - r_a}\right)\right]} \quad (4)$$

Tallman²⁹ and co-workers claimed that eq 2 is similarly accurate for the determination of currents for intermediate-sized rings,³⁰ and it is therefore used to normalize the simulated limiting currents for all ring sizes in the results given below, along with a further division by the maximum current obtained at a given flow rate, enabling results between different flow rates to be compared.

Figure 6 shows the results of increasing the inner radius of a ring electrode of $\Delta r = 56.5 \mu\text{m}$ on the limiting current for three different flow rates: 10^{-3} , 10^{-2} , and $10^{-1} \text{ cm}^3 \text{ s}^{-1}$. For each ring size, a comparison has been made between the semi-infinite wall case and $l_{\text{wall}} = 0.0125 \text{ cm}$. At all flow rates, as the electrode moves downstream, the limiting current increases, reaches a maximum, and then tails off. The current maximum is reached at a smaller r_a (and hence a smaller distance downstream) and is less broad as V_f is increased.

As in the case of the microdisk simulations, there is a degree of discrepancy between limiting currents obtained for the semi-infinite wall case and for a wall of the smallest thickness. Again, the discrepancy is larger at $V_f = 10^{-2} \text{ cm}^3 \text{ s}^{-1}$ than at flow rates 10 times larger or smaller, for reasons similar to those given for the microdisk case above. As the contours deviate more the further downstream they are, it might be expected that the largest difference in currents would be for large ring sizes, where the electrode is placed further and further downstream. From Figure 5, it can be seen that this is indeed the case. For all flow rates, the largest difference in current is at large values of r_a . It can also be noted from Figure 5 that for $V_f = 10^{-2}$ and $10^{-1} \text{ cm}^3 \text{ s}^{-1}$, close to the wall in which the ring electrode is embedded, the effect of reducing l_{wall} from the semi-infinite case to 0.0125 cm is to move those contours closer to the wall, which suggests higher speeds close to the wall and hence larger currents for $l_{\text{wall}} = 0.0125 \text{ cm}$. From inspection of Figure 5a, the opposite would be expected—the contours for $l_{\text{wall}} = 0.0125 \text{ cm}$ are further from the wall in which the electrode is embedded, and the slower velocities in that region would reduce the current

in comparison to that in the semi-infinite wall case. Figure 6 shows that this is indeed the case, the discrepancy between the two currents at each flow rate growing with increasing r_a . This is largest at $V_f = 10^{-2} \text{ cm}^3 \text{ s}^{-1}$, where the wall of thickness 0.0125 cm produces currents that are larger than in the semi-infinite wall case. This discrepancy grows from 3.5% at $r_a = 0.0113 \text{ cm}$ to 9.4% at $r_a = 0.22 \text{ cm}$. At $V_f = 10^{-1} \text{ cm}^3 \text{ s}^{-1}$, the currents are also larger for the thinner wall case, the discrepancy growing to 9.7% at $r_a = 0.22 \text{ cm}$, but for most ring sizes, the discrepancy is much smaller. For example, for $r_a < 0.17 \text{ cm}$, the discrepancy is always less than 0.2%. The opposite behavior is observed at $V_f = 10^{-3} \text{ cm}^3 \text{ s}^{-1}$: at high r_a , the currents for the $l_{\text{wall}} = 0.0125 \text{ cm}$ case are lower than for the semi-infinite wall case by 3.3%. Once again, for a given geometry and flow rate, the difference in limiting current between upper and lower exit placement was $<0.06\%$.

These results suggest that for a simple microdisk experiment in the MJE with the electrode centered directly below the inlet, nozzle-wall thickness has a negligible effect on limiting current, and the presence of a vortex above certain flow rates does not affect the flow to the electrode and hence the limiting current. However, it would appear from ring simulations that placing the electrode downstream results in currents sensitive to inlet wall geometry, and this effect can be augmented by the formation of vortices.

In an attempt to verify some of the observations made above, some simulated limiting ring currents were compared with experimental data obtained for a MJE cell with the electrode (of diameter $5 \mu\text{m}$) positioned off-center. Steady-state transport-limited currents were recorded at 296 K with $1 \text{ mM IrCl}_6^{3-}/\text{IrCl}_6^{2-}$ as the electroactive species. Relevant geometry and physical data are given in the second columns of Tables 1 and 2. Viscosities and densities were assumed to be the same as for 298 K because previous work²¹ has suggested that the effect of a 2 K change in temperature would be negligible.

The results for experiment are shown in Figure 7a, and the simulation results, in Figure 7b. Currents were normalized with respect to eq 2 for the simulated ring currents; in the case of the experimental work, the currents were normalized with respect to the standard steady-state diffusion current equation for a microdisk, eq 4.

As can be seen, the experimental results show the current passing through broad maxima as the electrode is displaced laterally with respect to the nozzle, as predicted by simulation. Also, the maxima occur at smaller displacements at higher flow rates, in agreement with simulation.

The ring simulations thus show the anticipated current maxima for off-set electrodes, although the qualitative relationship with microdisk experiments is limited. The latter is expected because the off-set microdisk experiment is a full 3D transport problem. Implicit in this discussion, however, is the need to analyze data from the latter type of experiment with caution, especially if vortices are likely to be developed.

Conclusions

FEM simulations have shown that the thickness of the inlet nozzle can have an effect on limiting currents obtained at the MJE. As a result, thicker nozzle walls are probably to be favored when considering the construction of MJE geometries; in the particular case above, a nozzle-wall thickness of 0.1625 cm would be expected to behave indistinguishably from the semi-infinite case, given typical experimental errors. The effects of changing l_{wall} on the currents is most pronounced if a vortex has been formed near the electrode and under some conditions

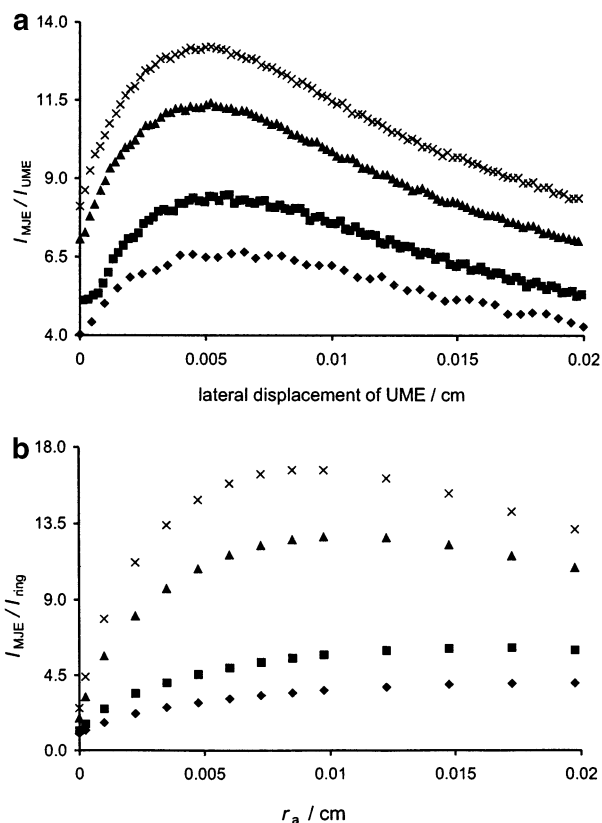


Figure 7. Limiting currents obtained for (a) experimental work with a microdisk of radius $2.5 \mu\text{m}$, moved progressively upstream, normalized with respect to the theoretical steady-state current in quiescent solution and (b) FEM simulation of a ring of $\Delta r = 2.5 \mu\text{m}$ with r_a progressively increased, normalized with respect to the Szabo steady-state ring equation. In both (a) and (b), the flow rates studied were $V_f = 8.33 \times 10^{-3} \text{ cm}^3 \text{ s}^{-1}$ (\blacklozenge), $V_f = 1.25 \times 10^{-2} \text{ cm}^3 \text{ s}^{-1}$ (\blacksquare), $V_f = 2.50 \times 10^{-2} \text{ cm}^3 \text{ s}^{-1}$ (\blacktriangle), and $V_f = 3.33 \times 10^{-2} \text{ cm}^3 \text{ s}^{-1}$ (\times).

could well provide a measurable effect on limiting currents. As vortex formation occurs at lower speeds for a larger nozzle–electrode separation, minimizing this distance will lead to a larger range of flow rates in which vortex-free flow will occur near the electrode. Alternatively, at higher speeds, the vortex forms further downstream and is therefore less likely to have an effect, at least for a microdisk positioned directly below the inlet. Therefore, it may be profitable to plan geometry based on the desired flow-rate range to be investigated in order to minimize the chance of vortex formation affecting the currents.

In terms of modeling, when simulating a microdisk, if the nozzle wall is of sufficient thickness, then the semi-infinite case can be applied, with exit placement being unimportant. This simplification of the cell geometry allows simulation over a

smaller volume, requiring shorter computational times. However, for ring electrodes, simplifications of this sort must be approached with caution—the presence of a vortex can considerably affect the flow downstream, and therefore a more exact simulation of cell geometry is required.

Acknowledgment. We thank EPSRC for a studentship for N.S. and J.L.M.

References and Notes

- (1) Macpherson, J. V.; Marcar, S.; Unwin, P. R. *Anal. Chem.* **1994**, *66*, 2175.
- (2) Macpherson, J. V.; Beeston, M. A.; Unwin, P. R. *J. Chem. Soc., Faraday Trans.* **1995**, *91*, 899.
- (3) Martin, R. D.; Unwin, P. R. *J. Electroanal. Chem.* **1995**, *397*, 2175.
- (4) Macpherson, J. V.; Unwin, P. R. *Anal. Chem.* **1997**, *69*, 2045.
- (5) Macpherson, J. V.; Simjee, N.; Unwin, P. R. *Electrochim. Acta* **2001**, *47*, 29.
- (6) Chin, D. T.; Tsang, C. H. *J. Electrochem. Soc.* **1978**, *125*, 1461.
- (7) Yamada, J.; Matsuda, H. *J. Electroanal. Chem.* **1973**, *44*, 189.
- (8) For a recent review, see Speiser, B. *Numerical Simulation—Recent Advances*. In *Electroanalytical Chemistry*; Bard, A. J., Rubinstein, I., Eds.; Marcel Dekker: New York, 1996; Vol. 19, p 1.
- (9) Whiting, L. F.; Carr, P. W. *J. Electroanal. Chem.* **1977**, *81*, 1.
- (10) Hertl, P.; Speiser, B. *J. Electroanal. Chem.* **1983**, *159*, 1.
- (11) Oldham, K. B. *Anal. Chem.* **1986**, *58*, 2296.
- (12) Friedrichs, M. S.; Friesner, R. A.; Bard, A. J. *J. Electroanal. Chem.* **1989**, *258*, 243.
- (13) Britz, D. *Digital Simulation in Electrochemistry*, 2nd ed.; Springer: Berlin, 1988.
- (14) Segerlind, L. J. *Applied Finite Element Analysis*, 2nd ed.; John Wiley: New York, 1984.
- (15) Fluent Europe Ltd., Sheffield, U.K. <http://www.fluent.com>.
- (16) Qiu, F.; Compton, R. G.; Coles, B. A.; Marken, F. *J. Electroanal. Chem.* **2000**, *492*, 150.
- (17) Marken, F.; Tsai, Y.-C.; Coles, B. A.; Matthews, S. L.; Compton, R. G. *New J. Chem.* **2000**, *24*, 653.
- (18) Beckmann, A.; Coles, B. A.; Compton, R. G.; Gruendler, P.; Marken, F.; Neudeck, A. *J. Phys. Chem. B* **2000**, *104*, 764.
- (19) Coles, B. A.; Compton, R. G.; Suarez, M.; Booth, J.; Hong, Q.; Sanders, G. H. W. *Langmuir* **1998**, *14*, 218.
- (20) Melville, J.; Simjee, N.; Unwin, P. R.; Coles, B. A.; Compton, R. G. *J. Phys. Chem. B* **2002**, *106*, 2690–2698.
- (21) Melville, J. L.; Coles, B. A.; Compton, R. G.; Simjee, N.; Macpherson, J. V.; Unwin, P. R. *J. Phys. Chem. B*, submitted for publication.
- (22) Albery, J. W.; Bruckenstein, S. *J. Electroanal. Chem.* **1983**, *144*, 105.
- (23) Macpherson, J. V.; Unwin, P. R. *Anal. Chem.* **1998**, *70*, 2914.
- (24) Macpherson, J. V.; Jones, C. E.; Unwin, P. R. *J. Phys. Chem. B* **1998**, *102*, 9891.
- (25) Unwin, P. R.; Compton, R. G. In *Comprehensive Chemical Kinetics*; Compton, R. G., Hammett, A., Eds.; Elsevier: Amsterdam, 1989; Vol. 29, p 173.
- (26) Szabo, A. *J. Phys. Chem.* **1987**, *91*, 3108.
- (27) Brookes, B. A.; Gavaghan, D. J.; Compton, R. G. *J. Phys. Chem. B* **2002**, *106*, 4886.
- (28) Symanski, J. S.; Bruckenstein, S. *J. Electrochem. Soc.* **1985**, *135*, 1985–1993.
- (29) Cope, D. K.; Scott, C. H.; Tallman, D. E. *J. Electroanal. Chem.* **1990**, *285*, 49.
- (30) Cooke, J. C. *Q. J. Appl. Math.* **1963**, *16*, 193.